

The Ghost of a Vanishing Stripe Order in the Triangular Quantum Ising Magnet

TmMgGaO₄

Han Li,¹ Yuan-Da Liao,^{2,3} Bin-Bin Chen,^{1,4} Xu-Tao Zeng,¹ Xian-Lei Sheng,¹ Yang Qi,^{5,*} Zi Yang Meng,^{2,3,6,7,†} and Wei Li^{1,8,‡}

¹*Department of Physics, Key Laboratory of Micro-Nano Measurement-Manipulation and Physics (Ministry of Education), Beihang University, Beijing 100191, China*

²*Beijing National Laboratory for Condensed Matter Physics, and Institute of Physics, Chinese Academy of Sciences, Beijing 100190, China*

³*School of Physical Sciences, University of Chinese Academy of Sciences, Beijing 100190, China*

⁴*Munich Center for Quantum Science and Technology (MCQST), Arnold Sommerfeld Center for Theoretical Physics (ASC) and Center for NanoScience (CeNS), Ludwig-Maximilians-Universität München, Fakultät für Physik, D-80333 München, Germany.*

⁵*Center for Field Theory and Particle Physics,*

Department of Physics, Fudan University, Shanghai 200433, China

⁶*Department of Physics, The University of Hong Kong, Hong Kong, China*

⁷*Songshan Lake Materials Laboratory, Dongguan, Guangdong 523808, China*

⁸*International Research Institute of Multidisciplinary Science, Beihang University, Beijing 100191, China*

(Dated: July 18, 2019)

Frustrated magnets host the promises of material realizations of new paradigm of quantum matter. However, due to their strongly correlated nature, direct comparison of unbiased model calculations with experiment results is still a challenge to the entire community. Here, we design and implement a protocol of employing quantum many-body computation methodologies – quantum Monte Carlo and thermal tensor network methods – to provide model exact calculation of both equilibrium and dynamical properties of a frustrated rare-earth magnet TmMgGaO₄ (TMGO) that perfectly explains the corresponding experimental findings. Our results confirm TMGO as an ideal realization of the transverse-field triangular lattice Ising model, and there emerge in its dynamical spectrum ghost images of the vanished magnetic stripe order, i.e., rotonlike excitation modes, representing the vortex-antivortex pair excitations. We propose the TMGO material realizes at finite temperature a Kosterlitz-Thouless (KT) phase resembling that in a superfluid helium film, and further suggest experimental detections of KT physics in this triangular quantum magnet.

* qiyang@fudan.edu.cn

† zymeng@iphy.ac.cn

‡ w.li@buaa.edu.cn

I. INTRODUCTION

Kosterlitz-Thouless (KT) physics bestows interesting mechanism of phase transition upon two-dimension (2D) interacting system with a continuous symmetry. Although spontaneous symmetry breaking does not happen at any finite temperature [1], the transition can still take place from the high temperature disordered phase to the quasi-long-range ordered KT phase, which has a topological root in the binding of the vortex and antivortex pairs [2, 3]. Experimentally, the KT transition has been observed in thin helium films [4, 5] and ultracold 2D bose gases [6–8]. Two distinct types of elementary excitations, i.e., phonons and rotons, play essential roles in the related superfluid phenomena [9, 10], and are important for the understanding of thermodynamics of the systems going through the KT transition [11, 12]. Besides interacting bosons, there are also theoretical proposals of KT transitions in magnetic systems such as the 2D XY model [2, 3] and the frustrated quantum Ising system [13, 14]. However, to date, the material realization of the KT transition in 2D magnets has been rare.

In the mean time, the search of exotic quantum magnetic states in the triangular lattice spin systems – the motif of frustrated magnets [15] – has attracted great attention over the decades [16, 17]. Experimentally, the triangular lattice quantum magnets have been synthesized rather late, in $\text{Ba}_3\text{CoSb}_2\text{O}_9$ [18–21] and $\text{Ba}_8\text{CoNb}_6\text{O}_{24}$ [22, 23], and a rare earth oxide YbMgGaO_4 – which has been suggested as a quantum spin liquid candidate [24–27], but alternative scenarios of glassy and disordered induced states have also been proposed recently [28–30]. However, by replacing Yb^{3+} with another rare earth ion Tm^{3+} , it is possible that an Ising-type triangular antiferromagnet TmMgGaO_4 [TMGO, shown in Fig. 1(a)] [31–33], as explained in details in this paper, is the successful material realization of a frustrated magnet hosting exotic KT physics. In this work we construct the correct model of TMGO and determine its microscopic parameters. We employ two state-of-the-art quantum many-body simulation techniques: the exponential tensor renormalization group (XTRG) [34] and quantum Monte Carlo equipped with stochastic analytical continuation (QMC-SAC) [35–39], to calculate both the thermodynamic and dynamic properties of TMGO. We fit the simulation results with the existing experimental data [31–33] and accurately determine the model parameters as $J_1 = 0.99$ meV, $J_2 = 0.05J_1$, $\Delta = 0.54J_1$ and $g_J = 1.101$ [see Eq. (1) below]. Moreover, we predict via precision quantum manybody simulations, prominent and experimentally accessible features close resemblance to the physics in a superfluid thin film in this 2D magnet.

It is worthwhile to point out that for the strongly correlated quantum material such as TMGO, only unbiased methods employed here could provide precise results, and we have found the parameter set obtained in Ref. [33] put the system in the disordered region of the phase diagram of Eq. (1), due to the inadequate treatment of quantum fluctuations in the linear-spin-wave approximation therein. Therefore, our methods

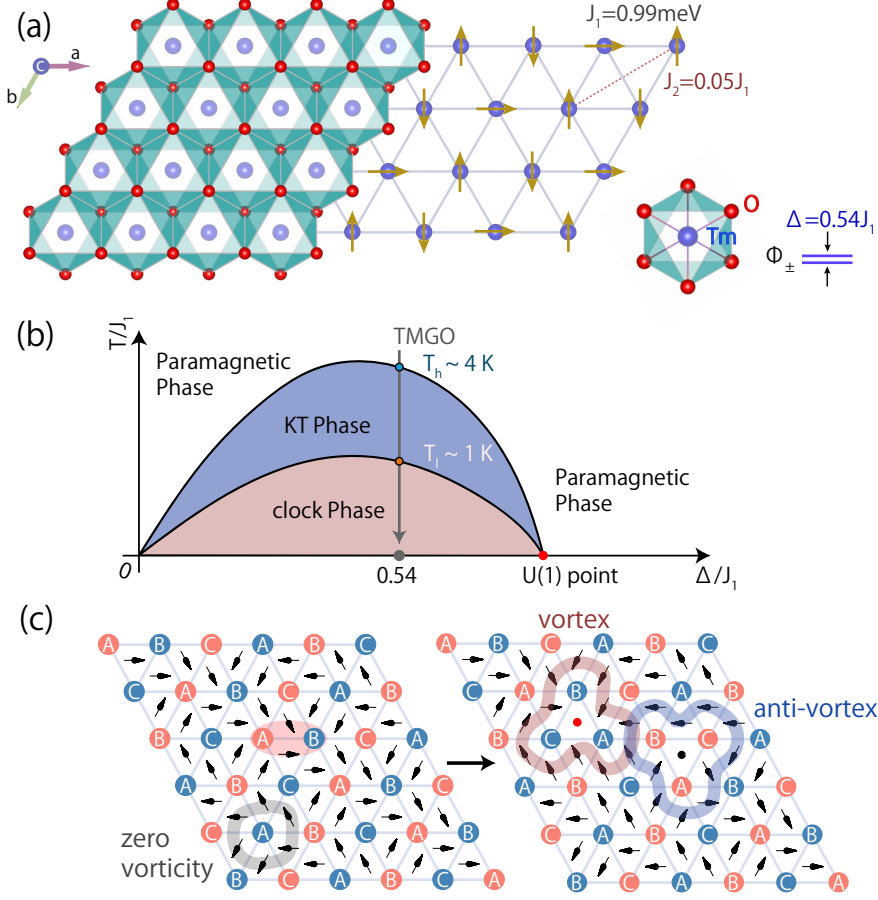


FIG. 1. The crystal structure and phase diagram of quantum TLI magnet TMGO. (a) The Tm^{3+} ions, with an energy splitting Δ between two lowest non-Kramers levels Φ_{\pm} , constitute a triangular lattice, with J_1 and J_2 interactions. (b) The phase diagram of quantum TLI model, where the vertical arrowed along $\Delta = 0.54J_1$ line represents the TMGO with two KT transitions (T_h and T_l). (c) shows the magnetic stripe order, with the red sites for spin-up and blue ones spin-down, on the three sublattices (A, B, and C). Pseudo spins, the order parameter ψ , are plotted as black arrows rotating within the plane, and a vortex-antivortex pair are created by flipping simultaneously the two spins within the red oven. Topological number ± 1 emerges when winding around the vortex/antivortex, while zero vorticity appears winding around both (or no defect at all).

and results not only explain the experimental findings of TMGO, but more importantly establish a protocol of acquiring equilibrium and dynamic experiments of frustrated magnets in an unbiased manner.

II. RESULTS

A. Model

As shown in Fig. 1, due to strong spin-orbit coupling and crystal electric field splittings in Tm^{3+} , TMGO can be described as an effective spin-1/2 model with a strong easy axis anisotropy, i.e., a triangular lattice Ising model (TLI). Partial electron density of 4f electrons in TMGO can be obtained from first-principle calculations (Supplementary Information), with effects of spin-orbit couplings and crystal fields included. It is observed that the 4f electron clouds of Tm^{3+} , mediated by 2p electrons of O^{2-} , show magnetic couplings within the 2D plane through triangular superexchange paths.

In Ref. [32], the authors took the lowest two levels in Tm^{3+} as non-Kramers doublet, and construct a classical triangular lattice Ising model (TLI) with both nearest-neighbor (NN) and next-nearest-neighbor (NNN) interactions to account for the absence of zero point entropy observed in experiments. Substantial randomness was also introduced to explain the smooth magnetization curves even at very low temperature. Later on, inelastic neutron scattering results of TMGO reveal a clear magnon band [33], suggesting the influence of coupling randomness should be modest in TMGO, and an adequate description of the material shall include non-commuting terms with quantum fluctuations. Since the Kramers theorem is absent in Tm^{3+} system with total angular momentum $J = 6$ (although the time-reversal symmetry is still present), there exists a quasi-doublet Φ_{\pm} with a small level splitting Δ , as shown in Fig. 1(a). Therefore, a quantum TLI model was proposed [33], with a Hamiltonian

$$H_{\text{TLI}} = J_1 \sum_{\langle i,j \rangle} S_i^z S_j^z + J_2 \sum_{\langle\langle i,j \rangle\rangle} S_i^z S_j^z - \sum_i (\Delta S_i^x + h g_{\parallel} \mu_B S_i^z), \quad (1)$$

where \langle , \rangle ($\langle\langle , \rangle\rangle$) stands for NN (NNN) couplings J_1 (J_2). Δ represents the energy splitting between two lowest levels, i.e., the intrinsic transverse field, and h is the external magnetic field. $g_{\parallel} = 2Jg_J$ constitutes the effective spin-1/2 g factor, with g_J the Landé factor. The phase diagram of quantum TLI has been studied intensively with analytic and numeric methods in the past [13, 14, 40] and is schematically shown in Fig. 1(b).

In the phase diagram, we indicate the TMGO model parameter with the vertical arrow (the determination of parameters is given below). From high to low temperatures, the system first goes through a transition at T_h from paramagnetic phase to a KT phase with power-law (algebraic) spin correlations. At a lower temperature T_l , the system experiences another KT transition and enters a clock phase with a true long-range order depicted in Fig. 1(a). This three-sublattice clock order breaks the discrete lattice point group as well as the Z_2 spin symmetries, leading to a low but finite transition temperature T_l .

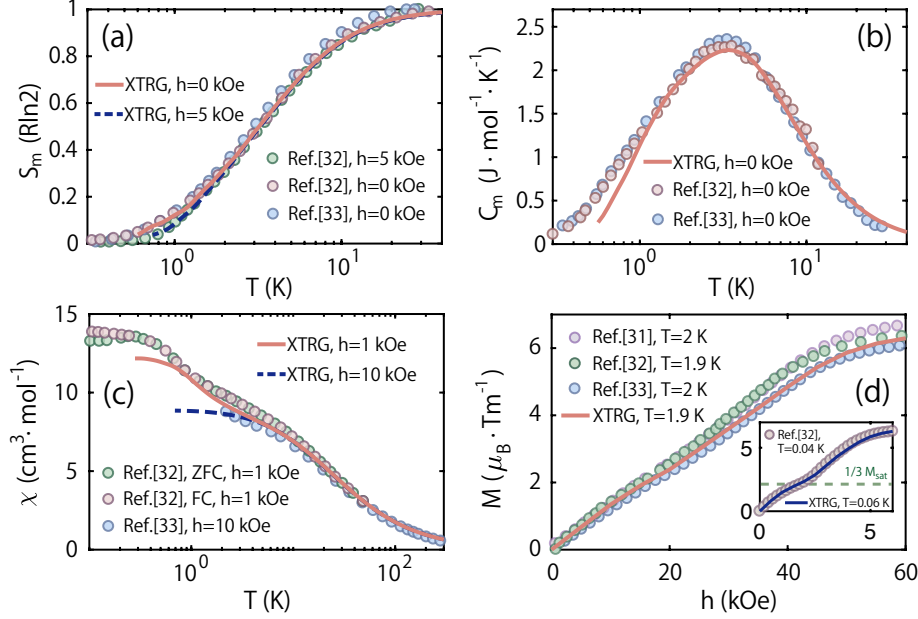


FIG. 2. Thermodynamics and XTRG fittings to experimental results. The comparisons of thermal quantities including (a) magnetic entropy, (b) specific heat, (c) susceptibility, and (d) magnetization are shown. The XTRG calculations are performed on YC9 lattices (see Supplementary Information) with parameters $J_1 = 0.99$ meV, $J_2 = 0.05 J_1$, $\Delta = 0.54 J_1$, and the Landé factor $g_J = 1.101$. Agreements between the experimental curves (taken from various independent measurements [31–33]) and numerical results can be seen in all panels, down to very low temperatures. (a) includes two experimental curves under $h = 0$ kOe and 5 kOe [32, 33] and (b) is under zero field only (see comparisons of nonzero-field C_m data in the Supplementary Information). In the χ curve in (c), from high to low temperatures, χ firstly increases according to Curie-Weiss law, $C/(T + \Theta)$ with $\Theta = -19$ K (see Supplementary Information). After that, there appears at ~ 10 K a shoulder structure in χ , signifying onset of the antiferromagnetic correlation. At about $T_h \sim 4$ K, the magnet enters the KT phase where χ rises up again, and as T decreases to around $T_l \sim 1$ K, the susceptibility eventually converges to a finite value. For the magnetization curves in (d), the perfect consistency between numerics and experiments hold for both intermediate $T \simeq 2$ K curves and one at 40 - 60 mK shown in the inset.

Increasing the next-nearest neighbor couplings J_2 , at $J_2/J_1 = 0.2$, we find the static magnetic structure factors develop a strip order peaks at the M point of the Brillouin zone (BZ), as shown in Fig. 1(c) (and see more details in Supplementary Information). This magnetic stripe order has been observed in an earlier studied TLI material AgNiO_2 [41], where the relatively strong J_2 coupling ($\sim 0.11 J_1$, along with other interactions) drives the systems into the stripe phase, with no KT phase appearing upon increasing T . In TMGO, however, the clock order wins over the stripe order as $J_2/J_1 \simeq 0.05$ in the material. Nevertheless, as will be shown below, a ghost of the latter – the M rotons – remains in the spin spectrum [33], which turns out to be related to a vortex-antivortex pair excitation in the topological language [see Fig. 1(c)].

B. Thermodynamics and parameter fittings

The model parameters of TMGO can be accurately determined through fitting the available experimental data [31–33]. We present in Fig. 2 the calculated $S_m(T)$, $C_m(T)$, $\chi(T)$ and their experimental counterparts, where excellent agreements are seen even down to the sub-Kelvin regime [32, 33]. In Fig. 2(a), at high temperatures $T > 30$ K, S_m approaches $R \ln 2$, corresponding to the paramagnetic phase with effective spin-1/2. As temperature decreases, the magnetic entropy S_m is gradually released throughout the intermediate temperature window of 1 K to 4 K, and at low $T < T_l \simeq 1$ K, S_m substantially reduces and approaches zero as the system freezes into the long-range clock order phase. In Fig. 2(b) the agreement in magnetic specific heat data C_m extends from high temperature (~ 30 K) all the way down to low $T \sim 0.8$ K, covering the entire paramagnetic and KT phases (and part of the clock phase).

In the fittings of the magnetic entropy and specific heat curves in Figs. 2(a,b), we adjust the x -axes (temperature T in the unit of J_1) to lay the model calculations on top of the experimental results, and in this way we find the optimized $J_1 = 0.99$ meV. In both plots, the y -axes are associated with the ideal gas constant $R = 8.313$ meV/K [note the additional $\ln(2)$ factor in the entropy curves in Fig. 2(a)], and are thus fixed. In Fig. 2(c), we fit the magnetic susceptibility $\chi = \frac{\partial M(h)}{\partial h}$, with $M(h)$ the uniform magnetization (per Tm^{3+}), under a small field $h = 1$ kOe and a slightly larger one of $h = 10$ kOe. As shown in Fig. 2(c), both measurements (under 1 and 10 kOe) can be fitted very well at the same time, by setting the Landé factor $g_J = 1.101$, completing the model parameter set in the Hamiltonian Eq. (1). Note that this Landé factor g_J also leads to the 5 kOe entropy results in Fig. 2(a) in excellent agreement with experimental line.

One remarkable feature in susceptibility χ is a two-step establishment of magnetic order [42, 43], as shown in Fig. 2(c). As pointed out in Refs. 42 and 43, an universal scaling $\chi(h) = h^{-\alpha}$ appears in the KT regime at small fields h , with $\alpha = \frac{4-18\eta(T)}{4-9\eta(T)}$, where $\eta(T) \in [\frac{1}{9}, \frac{2}{9}]$ is the anomalous dimension exponent of the emergent XY order parameter. The exponent varies with the temperature within the KT phase, $\eta = \frac{1}{9}$ for $T = T_l$ and $\chi(h) \sim h^{-2/3}$, diverging as h approaches zero; while for T_h , $\eta = \frac{2}{9}$ and $\chi(h) \sim h^0$ remains constant vs h . Therefore, at small external field ($h = 1$ kOe), the increase of χ at intermediate T is a consequence of the decrease of $\eta(T)$ vs. T , and such enhancement becomes less prominent for a relatively larger field $h = 10$ kOe. This salient difference indeed can be noticed in the experimental as well as our numerical curves in Fig. 2(c).

With the parameters J_1 , J_2 , Δ , and g_J determined from above fittings, we can compute the magnetization curve $M(T)$ and compare it directly with the experimental curves at various temperatures [31–33] in Fig. 2(d). Note there exists a turning point at a magnetic field of about 20 kOe, which corresponds to $\sim 1/3$ magnetization. This suggests the existence of a quantum phase transition driven by external fields and it

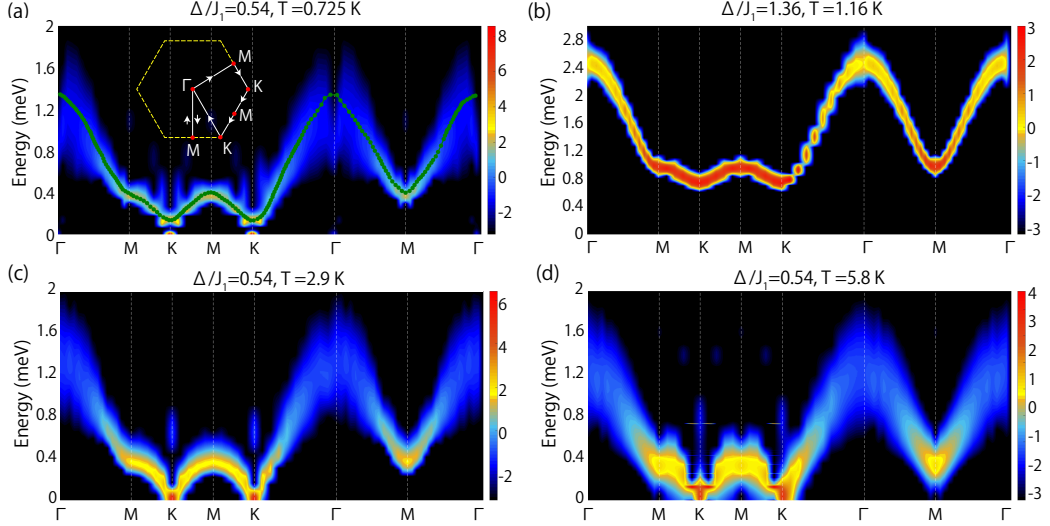


FIG. 3. QMC+SAC spectra of TMGO at finite temperature. (a) Spin spectrum calculated by QMC-SAC at $T = 0.725$ K, i.e., inside the clock phase, with the optimized parameter sets obtained from thermodynamic fittings in Fig. 2. The numerical spectrum agree excellently with the experimental neutron scattering results taken from Ref. [33], whose peak positions are denoted as the green dots. The path consists of the Γ - M - K - M - K - Γ loop and a Γ - M - Γ vertical mini-loop, as shown in the inset. (b) Spectrum with the parameter set given in Ref. [33], which clearly fails to describe the material. In (c,d) we plot in the spin spectra with model parameters in (a) but at higher temperatures, i.e., (c) $T = 2.9$ K inside the KT phase and (d) $T = 5.8$ K near the upper KT transition point. Compared to (a), the K point gap vanishes in panel (c) and the roton gap gets reduced in panel (d) – the linewidth near the roton minima is substantially broadened, suggesting vortex proliferation and strong fluctuation in the system.

becomes clearer as T decreases down to 40 mK, as shown the inset. Our XTRG results agree excellently with experimental data and reproduce the 1/3 quasi-plateau structure.

C. Spin spectra and magnetic structure factors

Frustration can lead to strong renormalization effects, which in turn gives rise to interesting spectrum. Here we employ the SAC-QMC approach [35–39] of the spin spectra $S(\mathbf{q}, \omega)$. The obtained spectra, with model parameters determined from equilibrium data fittings, are plotted in Fig. 3, and compared directly to inelastic neutron scattering (INS) results [33]. Fig. 3 (a) depicts the spin spectrum at low temperature $T = 0.725$ K, inside the clock phase as illustrated in Fig. 1(a). Since the clock phase is of discrete symmetry breaking, the $S(K, \omega = 0)$ signals the Bragg peak of the clock order and there exists a small gap between the $\omega = 0$ and finite ω spectra, as ~ 0.1 meV, consistent with the INS result. The roton modes at M -point are also clearly present in the SAC-QMC results, with an energy gap $\simeq 0.4$ meV, in quantitatively agreement

with that in Ref. [33].

Fig. 3(b) is the QMC-SAC spectrum calculated according to the parameters ($\Delta/J_1 \simeq 1.36$, $J_2/J_1 \simeq 0.046$) given in Ref. [33]. As mentioned in the introduction, we find, via spin structure factor calculations, that such set of parameters actually put the model in the disordered paramagnetic phase with $\Delta > \Delta_c \sim 0.8J_1$. It is possible that the fitting scheme adopted in Ref. [33] is based on mean-field treatment and cannot capture the quantum fluctuations inherent to the quantum TLI model as well as the TMGO material. This is a clear sign that the unbiased quantum many-body calculation scheme in our work is the adequate approach to explain the experimental results.

We continue with the parameter set in Fig. 3(a) and rise the temperature to $T = 2.9$ K within the KT phase in Fig. 3(c), as well as $T = 5$ K near the T_h in Fig. 3(d). It is interesting to see that the dispersion still resembles that in the clock phase of Fig. 3(a) but with a vanishing magnon gap at K , together with the gapped M roton modes, the dispersion resembles the renowned Landau's spectrum of liquid helium [44], such spectra provide a nontrivial prediction to be confirmed in future INS experiments. Furthermore, for T near T_h in Fig. 3(d), the roton gap is reduced with substantially broadened linewidth. Since M rotions can be related to vortex pair excitation [see Fig. 1(c) and discussions below], this “softening” of roton modes is consistent with the scenario of vortex proliferations near the upper KT transition $T_h \sim 4$ K.

Besides, the static magnetic structure factor $S(\mathbf{q}) = \sum_{i,j} e^{i\mathbf{q} \cdot (\mathbf{r}_i - \mathbf{r}_j)} \langle S_i^z S_j^z \rangle$ can also be simulated, where \mathbf{r}_i and \mathbf{r}_j run throughout the lattice. Fig. 4 (a) shows the temperature dependence of $S(K)$ and $S(M)$, where one observes an enhancement of $S(M)$ in the KT phase, signifying its closeness towards the stripe order. At temperatures lower than T_l , the enhancement of $S(M)$ vanishes and instead the $S(K)$ intensity becomes fully dominant. Figs. 4 (b,c) show the $S(\mathbf{q})$ results at low ($T = 0.57$ K) and an intermediate ($T = 2.2$ K) temperatures, i.e., inside the clock and KT phases, respectively. In the former case $S(\mathbf{q})$ evidently peaks at the K point, the ordering wavevector of the three-sublattice clock phase, while in the latter case, notably there exists a “ghost” peak at the M point, manifesting the existence of short-range stripe order selected by thermal fluctuations. These interesting ghost peak feature is gone at higher $T = 4.5$ K, where strong fluctuations near upper KT transition considerably broaden the K peaks.

D. Roton modes and the vortex-antivortex pair excitation

We ponder a bit more on the roton modes. As postulated by Landau, the phonon-roton spectrum play an important role in understanding thermodynamics and critical velocity of superfluid liquid helium, where the rotions are believed to be related with rotational motion of the fluid [9]. Roton constitutes a minimum in the spectrum at momentum k and finite energy, and are regarded as a quantum analog of hydrodynamic

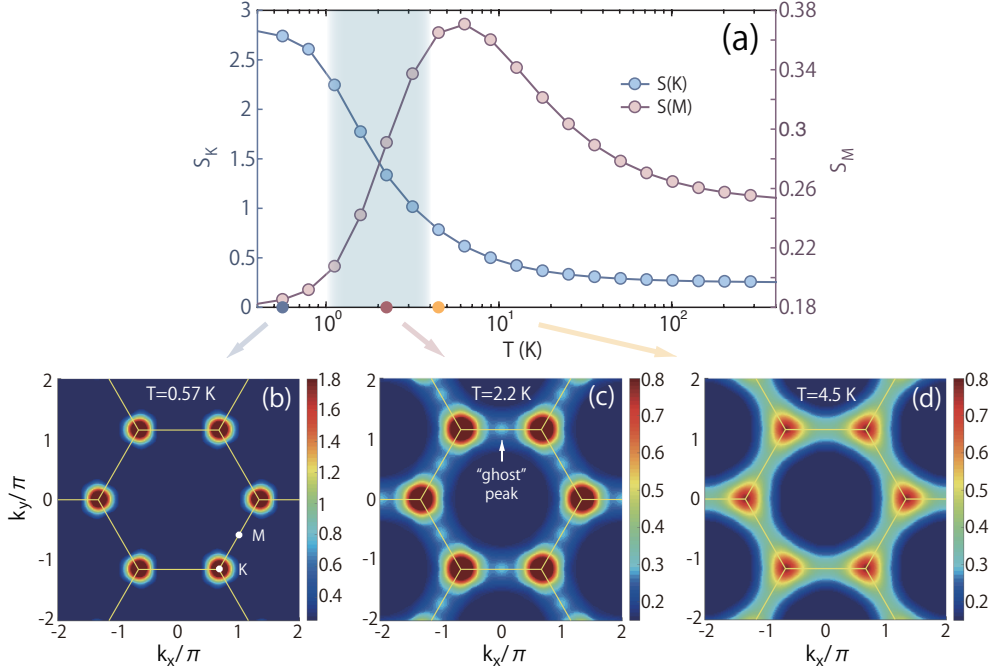


FIG. 4. Static magnetic structure factor of TMGO at finite temperatures. (a) The temperature dependence of the structure factor $S(\mathbf{q})$ at $\mathbf{q} = K, M$ calculated by XTRG on the YC9 lattice, $K = (1/3, 1/3)$ and $M = (1/2, 0)$, as indicated in panel (b). The $S(M)$ value enhances anomalously in the intermediate temperatures, while the K -point clock-order peak become significantly strengthened, representing the full establishment of the three sublattice clock order, at $T = 0.57$ K as shown in (b). Panel (c) shows the $S(\mathbf{q})$ contour at $T = 2.2$ K (inside the KT phase, marked as shaded regime), besides the dominant K -point peak, a “ghost” peak appears at M , due to populated rotons. In panel (d), as T further enhances to 4.5 K, near the upper KT transition, the K peak weakens and spreads out, with the M ghost peak becoming virtually invisible.

vortex ring [45], as coined “the ghost of vanished vortex ring” by Onsager [46]. As the excitation energy $\epsilon_k \sim \hbar k^2 / [2m S(k)]$, where m is the helium atom mass and $S(k)$ the structure factor, rotons have also been related to a vanishing crystallization Bragg peak $S(k)$ [47]. Rotonlike excitations are also found in systems with reduced dimensions, including the thin helium films [48] and frustrated triangular magnets [49, 50]. In the latter case, roton excitations strongly influence the thermodynamic properties at intermediate temperatures [34, 51], while its nature still remains to be revealed in terms of spin excitations.

As for the rotons in TMGO, on the other hand, we discover with a pseudo-spin mapping that it represents a pair of topological vortex excitations. Due to its intimate relation to the stripe order at M point, a proximate state strongly competing with the clock order while eventually gets perished at low T , the roton can be dubbed the “ghost” of the stripe order. Through a pseudo spin mapping, one arrives at

$$\psi = m_a^z + e^{i2\pi/3} m_b^z + e^{i4\pi/3} m_c^z, \quad (2)$$

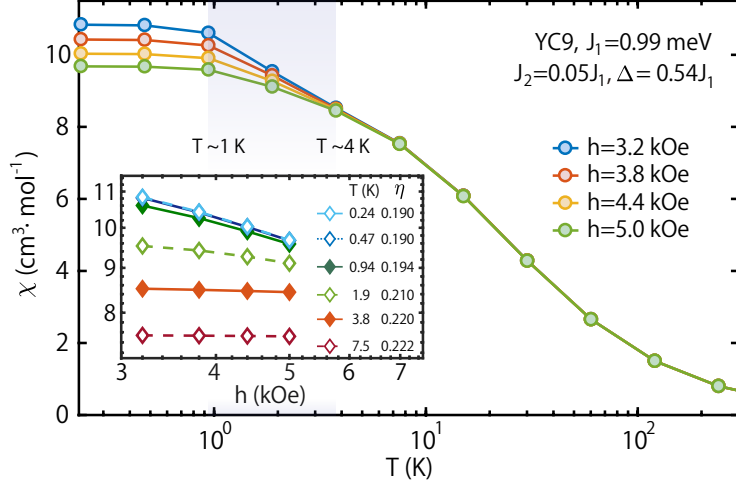


FIG. 5. Universal scaling of uniform magnetic susceptibility. At high temperature $T \gtrsim 4$ K, $\chi(h, T)$ remains independent of h for small fields, which indicates an exponent of $\alpha = 0$ in $\chi(h, T) \sim h^{-\alpha(T)}$, while for $1 \text{ K} \lesssim T \lesssim 4$ K (virtually the KT regime), $\chi(h, T)$ exhibits an algebraic scaling vs. h with $\alpha \neq 0$. For temperatures below the lower KT transition $T_l \sim 1$ K, the susceptibility ceases to increase as the system “freezes” into the clock phase. In the inset, $\chi(h, T)$ vs. h curves are presented in the log-log plot, where the algebraic scaling manifests itself in the KT phase (and in the clock phase due to the saturation). The fitted η values decrease from $2/9$ gradually to ~ 0.19 , the deviation of the latter from the expectation of $1/9$ at T_l is ascribed to limited lattice size (YC9) adopted in the XTRG calculations.

where $\psi = |\psi| e^{i\theta}$ is the complex order parameter [40], i.e., the pseudo spin located in the center of each triangle as shown in Fig. 1(c), with emergent XY degree of freedom θ . In Eq. (2), $m_\gamma^z = \pm 1$ represents the spin-up(-down) of corresponding spin configuration at γ -sublattice ($\gamma = a, b, c$).

From the mapping, we can see clearly in Fig. 1(c) that a vortex-antivortex pair defect with $|\psi| = 0$ can be created by applying S^x operator on two adjacent sites to flip their spin orientations. We can further move one of the vortices by flipping spins on further neighboring sites, giving rise to a quadratic-type dispersion near M point along the path selected in Fig. 3. Further, we note that any closed loop enclosing only the vortex defect [red dot in Fig. 1(c)] leads to a winding number 1 (modulo 2π), while those around the anti-vortex (black dot) to -1 . Zero winding number can be counted when a pair of defects (or no defects at all) are enclosed by the loop. As well-established, vortex excitations are key ingredients for realizing KT transition [2, 3], and the rotons in TMGO spectrum should be bounded vortex pairs, which unbind at upper KT transition temperature and the “superfluidity-normal” transition takes place. This scenario of vortex excitation proliferation is confirmed by the dynamical spectrum in Fig. 3(d).

III. DISCUSSION

In this work, we show, through large-scale quantum many-body calculations, that quantum TLI model can explain the experimental observations of TMGO, in particular the KT physics and roton excitations in thermodynamic and dynamic results are captured to great accuracy. We have corrected the over-estimated parameter sets in the previous work due to inadequate mean-field approximation and established a protocol of understanding and explaining experiments of frustrated magnets in an unbiased manner, with XTRG and QMC-SAC machinery. Along the temperature axis shown in Fig. 1(b), TMGO is in the KT phase for $T_l < T < T_h$, realizing a magnetic analog of the 2D superfluidity with several intriguing properties: (i) there emerges spin XY symmetry and correspondingly a complex order parameter ψ , which bears quasi-long-range correlation and phase coherence; (ii) the finite- T spin spectrum contains the long-wave-length soft magnon modes near the K point, and roton modes at finite momentum with energy signifying the binding of vortex-antivortex pair, very much similar to the phonon-roton spectrum in superfluid helium film; (iii) as T is above the upper transition T_h , the quasi-long range order melts and the TMGO becomes paramagnetic, similar as the superfluid-normal transition in helium film also driven by the proliferation of vortex excitations [4, 5].

Experimentally, the measurements of anomalous exponents $\eta(T)$ in the KT phase is a possible direction. To facilitate further experimental studies, we plot in Fig. 5 the susceptibility curves at various magnetic fields h (between 3.2 and 5.0 kOe), where the scaling is shown explicitly, with the exponent $\eta(T)$ extracted within the KT range as proposed in Refs. [42, 43]. Moreover, now that TMGO materializes a magnetic analog of the superfluid helium film, it would be interesting to check several predictions of KT physics in this magnetic platform. One renowned prediction is the universal jump in superfluid density at the KT transition [4, 52], which has been revealed numerically in the q -clock model ($q = 5, 6$) through the calculation of spin stiffness [53], and now is experimentally accessible in TMGO. Spin resonance measurements can be conducted to probe dynamical signals of magnetic dissipations in the KT phase, particularly near the upper KT transitions where vortices proliferate. Besides, non-equilibrium thermodynamics, e.g., the thermal transport of TMGO, would also be very worthwhile to explore both theoretically and experimentally in future studies.

METHODS

In this work, we combined two quantum many-body numerical approaches: quantum Monte Carlo (QMC) [40] and the exponential tensor renormalization group (XTRG), the latter is recently introduced

based on matrix product operators (MPOs) and logarithmic temperature scales [34, 54, 55]. XTRG is employed to simulate the TLI down to temperatures $T < 0.5$ K on $YC W \times L$ geometries [Supplementary Information] up to width $W = 9$ with various lengths, $L = 9, 12, 15$. Both dynamical and equilibrium properties are simulated, with the purpose of fitting the experimental data and obtaining the right parameters as well as to make some predictions. The QMC is performed in the space-time lattice of $L \times L \times L_\tau$, where $L = 30$ and $L_\tau = \beta/\Delta\tau$ with $\Delta\tau = 0.05$ and $\beta \equiv 1/T$. The space-time configuration is written in the $S_{i,\tau}^z$ basis with both local and Wolff-cluster updates to overcome the long autocorrelation time. Since the QMC method is standard, we will only introduce the stochastic analytic continuation (SAC) scheme here and leave the QMC itself to the Supplementary Information.

A. Exponential thermal tensor network method

For the calculations of equilibrium properties, we start from an high- T density matrix $\hat{\rho}(\Delta\tau) = e^{-\Delta\tau H}$, whose MPO representation can be obtained conveniently and accurately (up to machine precision), at a small $\Delta\tau \sim 10^{-3\sim-4}$. One way to obtain such an accurate MPO representation is

$$\hat{\rho}(\Delta\tau) = e^{-\Delta\tau \hat{H}} = \sum_{n=0}^{N_c} (-\Delta\tau)^n \hat{H}^n. \quad (3)$$

via the series-expansion thermal tensor network technique [55].

Given the $\hat{\rho}(\Delta\tau)$ representation, traditionally one evolves $\hat{\rho}(\beta)$ linear in β to lower temperatures, i.e., $\beta = L_\tau \Delta\tau$ increases by a small value $\Delta\tau$ after each step by multiplying $\hat{\rho}(\Delta\tau)$ to the density matrix. However, this linear scheme is not optimal in several aspects, and encounters challenges in generalization to 2D. Instead, recent study shows that the block entanglement entropy of MPO is bound by $S_E \leq a \ln \beta + const.$ at a conformal critical point, with a an universal coefficient proportional to the central charge [34]. This suggests an exponential procedure of performing cooling procedure. Based on this idea, we have developed the exponential tensor renormalization group method, which turns out to be highly efficient in both 1D critical quantum chains and various 2D lattice systems [34, 51, 56].

In XTRG, we cool down the system by multiplying the thermal state by itself, i.e., $\rho_0 \equiv \rho(\Delta\tau)$, $\rho_1 \equiv \rho_0 \cdot \rho_0 = \rho(2\Delta\tau)$, thus $\rho_n \equiv \rho_{n-1} \cdot \rho_{n-1} = \rho(2^n \Delta\tau)$, and reach the low- T thermal states exponentially fast. The compression of MPO bonds is then required to maintain the cooling procedure, where a truncation scheme optimizing the free energy, and in the mean time maintaining the thermal entanglement, is involved.

One advantage of XTRG is the convenience and high efficiency to deal with long-range interactions after the quasi-1D mapping. For the TLI model with nearest- (J_1) and next-nearest-neighbor (J_2) interactions considered in this work, we map the 2D lattice into a quasi-1D geometry following a snake-like path.

The Hamiltonian thus contains “long-range” interactions and has an efficient MPO representation with geometric bond dimension $D_H = 2W + 2$, with W the width of the lattice. In XTRG calculations, the computational costs scale with power $O(D^4)$, where D represents the retained bond states in MPO, which is chosen as large as 500-600 in the present study, assuring accurate thermodynamical results down to sub-Kelvin regime.

B. QMC+SAC

We exploit the path integral QMC [40], equipped with SAC approach, to compute the dynamical properties. The time displaced correlated function, defined as $S(\tau) = \langle S^z(\tau)S^z(0) \rangle$, for a set of imaginary times τ_i ($i = 0, 1, \dots, L_\tau$) with statistical errors can be obtained from QMC simulations. By SAC method [35, 36, 38, 39], the corresponding real-frequency spectral function $S(\omega)$ can be obtained via $S(\tau) = \int_{-\infty}^{\infty} d\omega S(\omega)K(\tau, \omega)$, where the kernel $K(\tau, \omega)$ depends on the type of the spectral function, i.e., fermionic or bosonic, finite or zero temperature. The spectra at positive and negative frequencies obey the relation of $A(-\omega) = e^{-\beta\omega}A(\omega)$ and we are restricted at the positive frequencies and the kernel can therefore be written as $K(\tau, \omega) = \frac{1}{\pi}(e^{-\tau\omega} + e^{-(\beta-\tau)\omega})$. In order to work with a spectral function that is itself normalized to unity, we further modify the kernel and the spectral function and arrive at the transformation between the imaginary time Green’s function $G(q, \tau)$ and real-frequency spectral function $B(q, \omega)$

$$G(q, \tau) = \int_0^{\infty} \frac{d\omega}{\pi} \frac{e^{-\tau\omega} + e^{-(\beta-\tau)\omega}}{1 + e^{-\beta\omega}} B(q, \omega) \quad (4)$$

where $B(q, \omega) = A(q, \omega)(1 + e^{-\beta\omega})$.

In the practical calculation, we parametrize the $B(\omega)$ with a large number of equal-amplitude δ -functions sampled at locations in a frequency continuum as $B(\omega) = \sum_{i=0}^{N_\omega-1} a_i \delta(\omega - \omega_i)$. Then the relationship between Green’s function obtained from Eq. (4) and from QMC can be described by the goodness of fit χ^2 , i.e. $\chi^2 = \sum_{i=1}^{N_\tau} \sum_{j=1}^{N_\tau} (G_i - \bar{G}_i) C_{ij}^{-1} (G_j - \bar{G}_j)$, where \bar{G}_i is the average of QMC measurement and C_{ij} is covariance matrix $C_{ij} = \frac{1}{N_B(N_B-1)} \sum_{b=1}^{N_B} (G_i^b - \bar{G}_i)(G_j^b - \bar{G}_j)$. N_B is the number of bins. Then we update the series of δ -functions in a Metropolis process, from (a_i, ω_i) to (a'_i, ω'_i) , to get a more probable configuration of $B(q, \omega)$. The weight for a given spectrum follows the Boltzmann distribution $P(B) \propto \exp(-\chi^2/2\Theta)$, with Θ a fictitious temperature chosen in an optimal way so as to give a statistically sound mean χ^2 value, while still staying in the regime of significant fluctuations of the sampled spectra so that a smooth averaged spectral function is obtained. The resulting spectra will be collected as an ensemble average of the Metropolis process within the configurational space of $\{a_i, \omega_i\}$, as detailed in Refs. 35, 36, 38, and 39.

Data availability. The data that support the findings of this study are available from the corresponding authors upon reasonable request.

- [1] N. D. Mermin and H. Wagner, “Absence of ferromagnetism or antiferromagnetism in one- or two-dimensional isotropic Heisenberg models,” *Phys. Rev. Lett.* **17**, 1133–1136 (1966).
- [2] J. M. Kosterlitz and D. J. Thouless, “Ordering, metastability and phase transitions in two-dimensional systems,” *J. Phys. C: Solid State Phys.* **6**, 1181–1203 (1973).
- [3] J. M. Kosterlitz, “The critical properties of the two-dimensional xy model,” *J. Phys. C: Solid State Phys.* **7**, 1046–1060 (1974).
- [4] D. J. Bishop and J. D. Reppy, “Study of the superfluid transition in two-dimensional ^4He films,” *Phys. Rev. Lett.* **40**, 1727–1730 (1978).
- [5] P. Minnhagen, “The two-dimensional coulomb gas, vortex unbinding, and superfluid-superconducting films,” *Rev. Mod. Phys.* **59**, 1001–1066 (1987).
- [6] Z. Hadzibabic, P. Krüger, M. Cheneau, B. Battelier, and J. Dalibard, “Berezinskii-Kosterlitz-Thouless crossover in a trapped atomic gas,” *Nature* **441**, 1118–1121 (2006).
- [7] P. Cladé, C. Ryu, A. Ramanathan, K. Helmerson, and W. D. Phillips, “Observation of a 2d bose gas: From thermal to quasicondensate to superfluid,” *Phys. Rev. Lett.* **102**, 170401 (2009).
- [8] R. Desbuquois, L. Chomaz, T. Yefsah, J. Léonard, J. and Beugnon, C. Weitenberg, and J. Dalibard, “Superfluid behaviour of a two-dimensional Bose gas,” *Nature Phys.* **8**, 645 (2012).
- [9] L. Landau, “On the theory of superfluidity,” *Phys. Rev.* **75**, 884–885 (1949).
- [10] R. P. Feynman, *Progress in Low Temperature Physics: Chapter II, Application of Quantum Mechanics to Liquid Helium*, edited by C. G. Gorter, Vol. 1 (North Holland, 1955).
- [11] H. C. Kramers, J. D. Wasscher, and C. J. Gorter, “The specific heat of liquid Helium between 0.25 and 1.9 K,” *Physica* **18**, 329 (1952).
- [12] P. J. Bendt, R. D. Cowan, and J. L. Yarnell, “Excitations in liquid Helium: Thermodynamic calculations,” *Phys. Rev.* **113**, 1386–1395 (1959).
- [13] R. Moessner, S. L. Sondhi, and P. Chandra, “Two-dimensional periodic frustrated Ising models in a transverse field,” *Phys. Rev. Lett.* **84**, 4457–4460 (2000).
- [14] S. V. Isakov and R. Moessner, “Interplay of quantum and thermal fluctuations in a frustrated magnet,” *Phys. Rev. B* **68**, 104409 (2003).
- [15] P. W. Anderson, “Resonating valence bonds: A new kind of insulator?” *Materials Research Bulletin* **8**, 153–160 (1973).
- [16] B. Bernu, C. Lhuillier, and L. Pierre, “Signature of Néel order in exact spectra of quantum antiferromagnets on finite lattices,” *Phys. Rev. Lett.* **69**, 2590–2593 (1992).
- [17] A. V. Chubukov, S. Sachdev, and T. Senthil, “Large-S expansion for quantum antiferromagnets on a triangular

- lattice,” *J. Phys.: Condens. Matter* **6**, 8891–8902 (1994).
- [18] Y. Doi, Y. Hinatsu, and K. Ohoyama, “Structural and magnetic properties of pseudo-two-dimensional triangular antiferromagnets $\text{Ba}_3\text{MSb}_2\text{O}_9$ ($\text{M} = \text{Mn, Co, and Ni}$),” *J. Phys.: Condens. Matter* **16**, 8923 (2004).
- [19] H. D. Zhou, C. Xu, A. M. Hallas, H. J. Silverstein, C. R. Wiebe, I. Umegaki, J. Q. Yan, T. P. Murphy, J.-H. Park, Y. Qiu, J. R. D. Copley, J. S. Gardner, and Y. Takano, “Successive phase transitions and extended spin-excitation continuum in the $S=\frac{1}{2}$ triangular-lattice antiferromagnet $\text{Ba}_3\text{CoSb}_2\text{O}_9$,” *Phys. Rev. Lett.* **109**, 267206 (2012).
- [20] T. Susuki, N. Kurita, T. Tanaka, H. Nojiri, A. Matsuo, K. Kindo, and H. Tanaka, “Magnetization process and collective excitations in the $S=1/2$ triangular-lattice Heisenberg antiferromagnet $\text{Ba}_3\text{CoSb}_2\text{O}_9$,” *Phys. Rev. Lett.* **110**, 267201 (2013).
- [21] G. Koutroulakis, T. Zhou, Y. Kamiya, J. D. Thompson, H. D. Zhou, C. D. Batista, and S. E. Brown, “Quantum phase diagram of the $S = \frac{1}{2}$ triangular-lattice antiferromagnet $\text{Ba}_3\text{CoSb}_2\text{O}_9$,” *Phys. Rev. B* **91**, 024410 (2015).
- [22] R. Rawl, L. Ge, H. Agrawal, Y. Kamiya, C. R. Dela Cruz, N. P. Butch, X. F. Sun, M. Lee, E. S. Choi, J. Oitmaa, C. D. Batista, M. Mourigal, H. D. Zhou, and J. Ma, “ $\text{Ba}_8\text{CoNb}_6\text{O}_{24}$: A spin- $\frac{1}{2}$ triangular-lattice Heisenberg antiferromagnet in the two-dimensional limit,” *Phys. Rev. B* **95**, 060412(R) (2017).
- [23] Y. Cui, J. Dai, P. Zhou, P. S. Wang, T. R. Li, W. H. Song, J. C. Wang, L. Ma, Z. Zhang, S. Y. Li, G. M. Luke, B. Normand, T. Xiang, and W. Yu, “Mermin-Wagner physics, (H, T) phase diagram, and candidate quantum spin-liquid phase in the spin- $\frac{1}{2}$ triangular-lattice antiferromagnet $\text{Ba}_8\text{CoNb}_6\text{O}_{24}$,” *Phys. Rev. Materials* **2**, 044403 (2018).
- [24] Y. Li, H. Liao, Z. Zhang, S. Li, F. Jin, L. Ling, L. Zhang, Y. Zou, L. Pi, Z. Yang, J. Wang, Z. Wu, and Q. Zhang, “Gapless quantum spin liquid ground state in the two-dimensional spin-1/2 triangular antiferromagnet YbMgGaO_4 ,” *Scientific Reports* **5**, 16419 (2015).
- [25] Y. Li, G. Chen, W. Tong, L. Pi, J. Liu, Z. Yang, X. Wang, and Q. Zhang, “Rare-earth triangular lattice spin liquid: A single-crystal study of YbMgGaO_4 ,” *Phys. Rev. Lett.* **115**, 167203 (2015).
- [26] Y. Li, D. Adroja, P. K. Biswas, P. J. Baker, Q. Zhang, J. Liu, A. A. Tsirlin, P. Gegenwart, and Q. Zhang, “Muon spin relaxation evidence for the $\text{U}(1)$ quantum spin-liquid ground state in the triangular antiferromagnet YbMgGaO_4 ,” *Phys. Rev. Lett.* **117**, 097201 (2016).
- [27] Y. Shen, Y.-D. Li, H. Wo, Y. Li, S. Shen, B. Pan, Q. Wang, H. C. Walker, P. Steffens, M. Boehm, Y. Hao, D. L. Quintero-Castro, L. W. Harriger, M. D. Frontzek, L. Hao, S. Meng, Q. Zhang, G. Chen, and J. Zhao, “Evidence for a spinon Fermi surface in a triangular-lattice quantum-spin-liquid candidate,” *Nature* **540**, 559 (2016).
- [28] Z. Zhu, P. A. Maksimov, S. R. White, and A. L. Chernyshev, “Disorder-induced mimicry of a spin liquid in YbMgGaO_4 ,” *Phys. Rev. Lett.* **119**, 157201 (2017).
- [29] I. Kimchi, A. Nahum, and T. Senthil, “Valence bonds in random quantum magnets: Theory and application to YbMgGaO_4 ,” *Phys. Rev. X* **8** (2018), 10.1103/physrevx.8.031028.
- [30] Z. Ma, J. Wang, Z.-Y. Dong, J. Zhang, S. Li, S.-H. Zheng, Y. Yu, W. Wang, L. Che, K. Ran, S. Bao, Z. Cai, P. Čermák, A. Schneidewind, S. Yano, J. S. Gardner, X. Lu, S.-L. Yu, J.-M. Liu, S. Li, J.-X. Li, and J. Wen, “Spin-glass ground state in a triangular-lattice compound YbZnGaO_4 ,” *Phys. Rev. Lett.* **120**, 087201 (2018).
- [31] F. A. Cevallos, K. Stolze, T. Kong, and R. J. Cava, “Anisotropic magnetic properties of the triangular plane

- lattice material TmMgGaO_4 ,” arXiv:1710.07707 (2018).
- [32] Y. Li, S. Bachus, Y. Tokiwa, A. A. Tsirlin, and P. Gegenwart, “Absence of zero-point entropy in a triangular Ising antiferromagnet,” arXiv:1804.00696 , arXiv:1804.00696 (2018).
- [33] Y. Shen, C. Liu, Y. Qin, S. Shen, Y.-D. Li, R. Bewley, A. Schneidewind, G. Chen, and J. Zhao, ““Hidden order” and its quantum excitations in the triangular-lattice magnet TmMgGaO_4 ,” arXiv:1810.05054 (2018), arXiv:1810.05054 [cond-mat.str-el].
- [34] B.-B. Chen, L. Chen, Z. Chen, W. Li, and A. Weichselbaum, “Exponential thermal tensor network approach for quantum lattice models,” Phys. Rev. X **8**, 031082 (2018).
- [35] A. W. Sandvik, “Constrained sampling method for analytic continuation,” Phys. Rev. E **94**, 063308 (2016).
- [36] Y. Q. Qin, B. Normand, A. W. Sandvik, and Z. Y. Meng, “Amplitude mode in three-dimensional dimerized antiferromagnets,” Phys. Rev. Lett. **118**, 147207 (2017).
- [37] H. Shao, Y. Q. Qin, S. Capponi, S. Chesi, Z. Y. Meng, and A. W. Sandvik, “Nearly deconfined spinon excitations in the square-lattice spin-1/2 Heisenberg antiferromagnet,” Phys. Rev. X **7**, 041072 (2017).
- [38] C.-J. Huang, Y. Deng, Y. Wan, and Z. Y. Meng, “Dynamics of topological excitations in a model quantum spin ice,” Phys. Rev. Lett. **120**, 167202 (2018).
- [39] G.-Y. Sun, Y.-C. Wang, C. Fang, Y. Qi, M. Cheng, and Z. Y. Meng, “Dynamical signature of symmetry fractionalization in frustrated magnets,” Phys. Rev. Lett. **121**, 077201 (2018).
- [40] Y.-C. Wang, Y. Qi, S. Chen, and Z. Y. Meng, “Caution on emergent continuous symmetry: A Monte Carlo investigation of the transverse-field frustrated Ising model on the triangular and honeycomb lattices,” Phys. Rev. B **96**, 115160 (2017).
- [41] E. M. Wheeler, R. Coldea, E. Wawryńska, T. Sörgel, M. Jansen, M. M. Koza, J. Taylor, P. Adroguer, and N. Shannon, “Spin dynamics of the frustrated easy-axis triangular antiferromagnet $2H\text{-AgNiO}_2$ explored by inelastic neutron scattering,” Phys. Rev. B **79**, 104421 (2009).
- [42] K. Damle, “Melting of three-sublattice order in easy-axis antiferromagnets on triangular and kagome lattices,” Phys. Rev. Lett. **115**, 127204 (2015).
- [43] S. Biswas and K. Damle, “Singular ferromagnetic susceptibility of the transverse-field Ising antiferromagnet on the triangular lattice,” Phys. Rev. B **97**, 085114 (2018).
- [44] E. M. Lifshitz and L. P. Pitaevskii, *Statistical Physics, Part 2* (Butterworth-Heinemann, Oxford, 1980) Chap. 3.
- [45] R. P. Feynman, “Atomic theory of the two-fluid model of liquid Helium,” Phys. Rev. **94**, 262–277 (1954).
- [46] R. J. Donnelly, “The ghost of a vanished vortex ring,” in *Quantum Statistical Mechanics in the Natural Sciences: A Volume Dedicated to Lars Onsager on the Occasion of his Seventieth Birthday*, edited by Stephan L. Mintz and Susan M. Widmayer (Springer US, Boston, MA, 1974) pp. 359–402.
- [47] P. Nozières, “Is the roton in superfluid He^4 the ghost of a Bragg spot?” J. Low Temp. Phys. **137**, 45–67 (2004).
- [48] K. Carneiro, W. D. Ellenson, L. Passell, J. P. McTague, and H. Taub, “Neutron-scattering study of the structure of adsorbed Helium monolayers and of the excitation spectrum of few-atomic-layer superfluid films,” Phys. Rev. Lett. **37**, 1695 (1976).
- [49] J. Ma, Y. Kamiya, T. Hong, H. B. Cao, G. Ehlers, W. Tian, C. D. Batista, Z. L. Dun, H. D. Zhou, and M. Matsuda,

- “Static and dynamical properties of the spin-1/2 equilateral triangular-lattice antiferromagnet $\text{Ba}_3\text{CoSb}_2\text{O}_9$,” *Phys. Rev. Lett.* **116**, 087201 (2016).
- [50] S. Ito, N. Kurita, H. Tanaka, S. Ohira-Kawamura, K. Nakajima, S. Itoh, K. Kuwahara, and K. Kakurai, “Structure of the magnetic excitations in the spin-1/2 triangular-lattice Heisenberg antiferromagnet $\text{Ba}_3\text{CoSb}_2\text{O}_9$,” *Nature Commun.* **8**, 235 (2017).
- [51] L. Chen, D.-W. Qu, H. Li, B.-B. Chen, S.-S. Gong, J. von Delft, A. Weichselbaum, and W. Li, “Two temperature scales in the triangular lattice Heisenberg antiferromagnet,” *Phys. Rev. B* **99**, 140404(R) (2019).
- [52] D. R. Nelson and J. M. Kosterlitz, “Universal jump in the superfluid density of two-dimensional superfluids,” *Phys. Rev. Lett.* **39**, 1201–1205 (1977).
- [53] C. Chatelain, “DMRG study of the Berezinskii–Kosterlitz–Thouless transitions of the 2D five-state clock model,” *Journal of Statistical Mechanics: Theory and Experiment* **2014**, P11022 (2014).
- [54] W. Li, S.-J. Ran, S.-S. Gong, Y. Zhao, B. Xi, F. Ye, and G. Su, “Linearized tensor renormalization group algorithm for the calculation of thermodynamic properties of quantum lattice models,” *Phys. Rev. Lett.* **106**, 127202 (2011).
- [55] B.-B. Chen, Y.-J. Liu, Z. Chen, and W. Li, “Series-expansion thermal tensor network approach for quantum lattice models,” *Phys. Rev. B* **95**, 161104(R) (2017).
- [56] H. Li, B.-B. Chen, Z. Chen, J. von Delft, A. Weichselbaum, and W. Li, “Thermal tensor renormalization group simulations of square-lattice quantum spin models,” *Phys. Rev. B* **100**, 045110 (2019).
- [57] G. Kresse and J. Furthmüller, “Efficient iterative schemes for ab initio total-energy calculations using a plane-wave basis set,” *Phys. Rev. B* **54**, 11169–11186 (1996).
- [58] G. Kresse and D. Joubert, “From ultrasoft pseudopotentials to the projector augmented-wave method,” *Phys. Rev. B* **59**, 1758–1775 (1999).

ACKNOWLEDGEMENTS

This work was supported by the Ministry of Science and Technology of China through the National Key Research and Development Program (Grant No. 2016YFA0300502), the Strategic Priority Research Program of the Chinese Academy of Sciences (Grant No. XDB28000000), and the National Science Foundation of China (Grant No. 11421092, 11574359, 11674370 and 11834014). B.-B.C. was supported by the German Research foundation, DFG WE4819/3-1. W.L. was supported by the Fundamental Research Funds for the Central Universities. We thank the Center for Quantum Simulation Sciences at Institute of Physics, Chinese Academy of Sciences, and the Tianhe-1A platform at the National Supercomputer Center in Tianjin and the Tianhe-2 platform at the National Supercomputer Center in Guangzhou for their technical support and generous allocation of CPU time.

SUPPLEMENTARY INFORMATION

C. The electron density distributions

Density-functional theory (DFT) calculations of TMGO in the present work are performed via the Vienna *ab initio* simulation package, with the projector augmented wave method [57, 58]. In the DFT calculations, we take the TMGO lattice parameters $a = b = 3.4260 \text{ \AA}$ and $c = 25.1690 \text{ \AA}$ as determined from experiments.

Without on-site Coulomb interactions U , the band structure of TMGO indicates a metallic state [Fig. S1(a)], while a finite $U = 2 \text{ eV}$ opens a Mott gap as shown in Fig. S1(b). The partial electron density results relevant for magnetic interactions include the contributions of 4f electrons of Tm^{3+} and 2p electrons of O^{2-} , which are hybridized (as seen in the density of states between energies of 1 and 1.6 eV). The triangular lattice formed by Tm^{3+} are visualized via the Tm-O-Tm superexchange paths. Through this intuitive picture, we reveal that the magnetic interactions between 4f electrons are mediated via 2p electrons, i.e., a superexchange mechanism. The two dimensionality of the material TMGO is also manifested, since the electron density at the interlayer middle point (A in Fig. S1) between two Tm ions is 4 orders of magnitude smaller than that of B point (a typical point in Tm-O-Tm path).

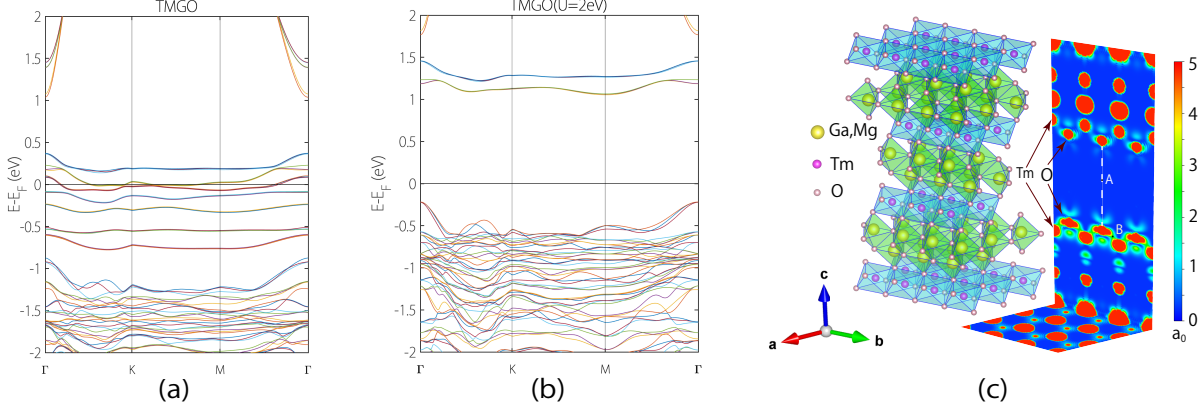


Fig. S1. The layered crystal structure and partial electron density distributions. (a,b) show the energy band results, with and without U , calculated by DFT. (c) is the lattice structure of TMGO, where a_0 denotes 10^{-6} e/Bohr^3 . The partial electron density plot within energy between 1 eV and 1.6 eV is also plotted in (c), where 4f electrons of Tm^{3+} and 2p electrons of O^{2-} contribute mainly the density of states. The two dimensionality of magnetic couplings in TMGO can be seen by checking the electron densities at point A (between two layers) and B [a typical point in the superexchange path within the (001) plane], which are different by 4 orders of magnitude.

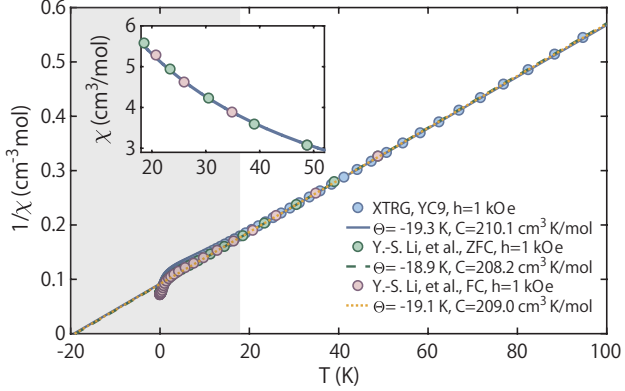


Fig. S2. The Curie-Weiss behavior at high temperature. Here we show the high- T susceptibility data and study its Curie-Weiss behavior $\chi = \frac{C}{T - \Theta_W}$, with $C \simeq 210.1 \text{ K cm}^3/\text{mol}$ the Curie constant and $\Theta_W \simeq -19 \text{ K}$ the Curie-Weiss temperature. The blue circles represent the inverse susceptibility χ^{-1} vs. T , and the χ vs. T curve is plotted in the inset. The XTRG susceptibility χ is computed with model parameters $J_1 = 0.99 \text{ meV}$, $J_2 = 0.05J_1$, $\Delta = 0.54J_1$, and $h = 1 \text{ kOe}$, on a $YC9 \times 12$ lattice. The Curie-Weiss fittings are done within the temperature range $T \in [6, 48] \text{ K}$ (experiments, FC and ZFC), and $T \in [18, 100] \text{ K}$ (XTRG curve), i.e., high temperature data on the right of the grey shaded regime.

D. Curie-Weiss Fittings

As a complementary of the thermodynamic fittings in the main text, we compare the high-temperature data of magnetic susceptibility in Fig. S2, where virtually no finite-size effects are noticeable. In Fig. S2, the $\Delta/J_1 = 0.54$ line lay on top of two experimental curves, with fitted $\Theta_W \sim 19.3 \text{ K}$, in very good agreement with the estimates in experimental works (e.g., 18.9 - 19.1 K as indicated in the plot). Besides, the fitted constant $C \simeq 210.1 \text{ K cm}^3/\text{mol}$, which leads to an estimate of the Landé factor $g_J = \frac{1}{12\sqrt{S(S+1)}\mu_B}\frac{\sqrt{3k_B C}}{\sqrt{N_A\mu_0}} = 1.1$, where $S = 1/2$ represents the effective spin-1/2. This g_J value agrees with the Landé factor 1.101 obtained in the main text, thus constituting a self-consistency check of our thermodynamics fittings.

To conclude, after simulations of both equilibrium and dynamical properties, we pinpoint the model parameters of TMGO as $J_1 = 0.99 \text{ meV}$, $\Delta/J_1 = 0.54$, $J_2/J_1 = 0.05$, and $g_J \simeq 1.101$, which can be used to fit virtually all available experimental data, including the magnetic specific heat, susceptibility (both high- and low-temperature parts), and spin spectrum, etc.

E. Spin ordering and phase diagram of the J_1 - J_2 TLI

As mentioned in the main text, that increasing the ratio of J_2/J_1 could drive the system from clock order phase to a stripe order phase. To verify this picture, we calculate the static magnetic structure factor $S(\mathbf{q})$

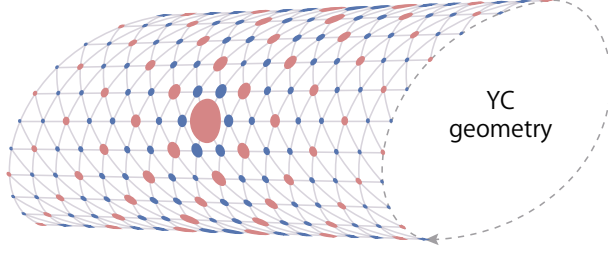


Fig. S3. Real-space $\langle S_0^z \cdot S_r^z \rangle$ correlation and a three-sublattice order. Each solid circle represents the real-space $\langle S_0^z \cdot S_r^z \rangle$ correlation related to the central site, the size of circle denotes the magnitude of correlation, and the red(blue) color for the positive(negative) sign. The clock order pattern with enlarged unit cell can be clearly seen. The XTRG calculation is performed with parameters $J_1 = 0.99$ meV, $J_2 = 0.05J_1$, and $\Delta = 0.54J_1$ at $T \simeq 0.57$ K, on the YC geometry also explicitly specified in the plot.

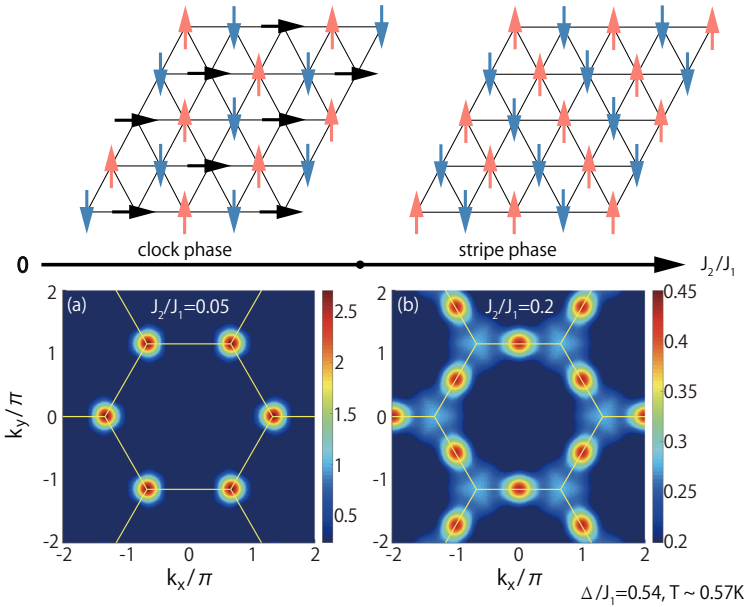


Fig. S4. Schematic phase diagram of the $J_1 - J_2$ TLI and static structure factors. As J_2 increases, there exists a quantum phase transition between the clock and stripe phases, taking place at $J_2/J_1 \sim 0.1$ (for $\Delta/J_1 = 0.54$). The magnetic structure factors for two phases, measured at a low temperature $T = 0.57$ K, are shown in panels (a) and (b), with the former has Bragg peak at K and the latter at M , respectively.

in XTRG, shown in Fig. S4. It is clear here that at $J_2/J_1 = 0.05$ the $S(\mathbf{q})$ is peaked at the K point (the bright spot at the zone center comes from the conservation of spin and is not related with the order at Γ), signifying the presence of clock phase. However, at $J_2/J_1 = 0.2$, $S(\mathbf{q})$ is peaked at M -point, which is consistent with the real space stripe orientation of the S_i^z in right panel above the phase diagram. Therefore the M -point is the ordered wavevector of the stripe phase and the transition between clock and stripe phases is at $J_2/J_1 \sim 0.1$. Due to the finite size of XTRG, we couldn't distinguish the order of the transition but

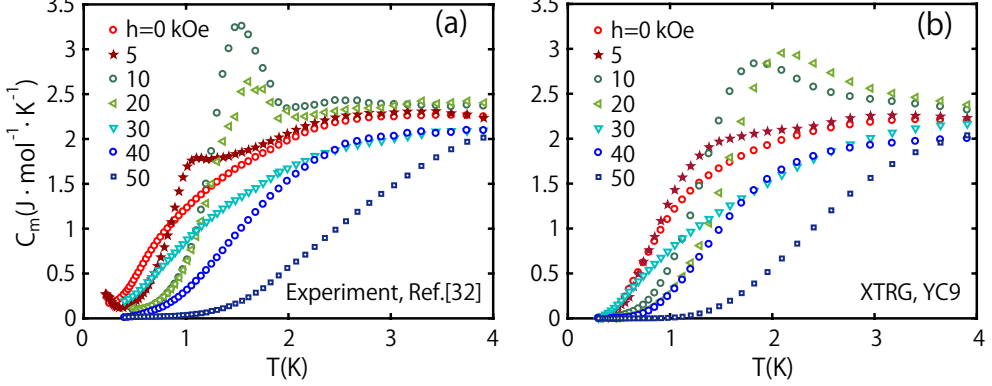


Fig. S5. Specific heat curves under magnetic fields. (a) shows the experimental specific heat data under various magnetic fields, taken from Ref. [32], and (b) is the corresponding XTRG results. Despite that the peak in C_m between 1K and 2K are less pronounced in the simulated results than experiments, under $h = 5, 10$ and 20 kOe, the comparisons are in quite good consistency, suggesting the correctness of the parameter sets and the accuracy of XTRG calculations.

it is most likely a first one. And the dynamic spin spectra showed in the main text, with finite energy roton excitations at the M -point, is the ghost image of the stripe order.

F. Specific heat curves under external fields

As has been noted earlier in Fig. 2(d) in the main text, the magnetization curves $m(T)$ show a weak plateau at $m/m_{sat} \simeq 1/3$, where m_{sat} is the saturation magnetization along the z direction. In Ref. [32], the specific heat curves have also been measured under various external magnetic fields. In Fig. S5(b), we plot the simulated $C_m(h, T)$ curves and compare them, side by side, to the measured data redrawn in Fig. S5(a). It can be seen clearly that in both Figs. S5(a) and (b), a low- T shoulder gradually appears under small fields, e.g., $h = 5$ kOe, and it becomes prominent peaks at around $h = 10\text{-}20$ kOe.

It is remarkable that these highly nontrivial and non-monotonic behaviors of $C_m(h, T)$ curves can also be understood within the TLI model. As shown in Fig. 2(d) of the main text, there exists a quasi-plateau structure at about $1/3 M_{sat}$ in the curve, which suggests that the system undergoes a transition from the clock order to an up-up-down (UUU) spin state upon increasing fields to $h = 10\text{-}20$ kOe. The forming of the UUU structure releases entropy and gives rise to the prominent low- T peak in C_m . As the field strength further increases, the UUU order becomes weaker and accordingly the C_m peak moves back to lower T side with a decreasing height. Eventually, for $h > 30$ kOe, the system gradually polarizes into a ferromagnetic spin configuration, and the C_m peaks merges into a hump moving towards higher T as h enhances.

G. Brief introduction of path integral QMC for TLI

The Hamiltonian of quantum TLI is $\mathcal{H} = J_1 \sum_{\langle i,j \rangle} S_i^z S_j^z + J_2 \sum_{\langle\langle i,j \rangle\rangle} S_i^z S_j^z - h \sum_i S_i^x$ where, the external magnetic field part is omitted for clearance of narrative.

QMC evaluate the partition function $Z = \text{Tr} [e^{-\beta \mathcal{H}}]$, to efficiently evaluate the trace, discretized imaginary time is used and $\beta = L_\tau \Delta\tau$ ($\Delta\tau = 0.05$) in this work. And the partition function of the Hamiltonian can be mapped onto that of a (2+1)D classical system as follows,

$$\begin{aligned} Z &= \text{Tr} [e^{-\beta \mathcal{H}}] \\ &= \text{Tr} [e^{-\Delta\tau \mathcal{H}} e^{-\Delta\tau \mathcal{H}} \cdots e^{-\Delta\tau \mathcal{H}} e^{-\Delta\tau \mathcal{H}}] \end{aligned} \quad (\text{S1})$$

Now, by inserting a complete set of S_i^z eigenstates between each pair of exponentials, i.e.,

$$\begin{aligned} 1 &= \prod_{i=1}^N \left[\sum_{S_i^z=\pm 1} |S_i^z\rangle \langle S_i^z| \right] \\ &\equiv \sum_{\{S_i^z\}} |S^z\rangle \langle S^z|, \end{aligned} \quad (\text{S2})$$

we can thus rewrite the partition function as,

$$\begin{aligned} Z &= \sum_{\{S_{i,l}\}=\pm 1} \langle S_1^z | e^{-\Delta\tau \mathcal{H}} | S_L^z \rangle \langle S_L^z | e^{-\Delta\tau \mathcal{H}} | S_{L-1}^z \rangle \langle S_{L-1}^z | e^{-\Delta\tau \mathcal{H}} | S_{L-2}^z \rangle \cdots \\ &\quad \cdots \langle S_3^z | e^{-\Delta\tau \mathcal{H}} | S_2^z \rangle \langle S_2^z | e^{-\Delta\tau \mathcal{H}} | S_1^z \rangle, \end{aligned} \quad (\text{S3})$$

where l indices the time slice $\tau = l \cdot \Delta\tau$. Now, we can employ the Trotter-Suzuki decomposition,

$$\begin{aligned} \langle S_{l+1}^z | e^{-\Delta\tau \mathcal{H}} | S_l^z \rangle &= \langle S_{l+1}^z | e^{-\Delta\tau \mathcal{H}_1 - \Delta\tau \mathcal{H}_0} | S_l^z \rangle \\ &= \langle S_{l+1}^z | e^{-\Delta\tau \mathcal{H}_1} e^{-\Delta\tau \mathcal{H}_0} | S_l^z \rangle + O[(\Delta\tau)^2]. \end{aligned} \quad (\text{S4})$$

Here, $\mathcal{H}_0 = J_1 \sum_{\langle i,j \rangle} S_i^z S_j^z + J_2 \sum_{\langle\langle i,j \rangle\rangle} S_i^z S_j^z$, $\mathcal{H}_1 = -h \sum_i S_i^x$, and the matrix element becomes,

$$\langle S_{l+1}^z | e^{-\Delta\tau \mathcal{H}_1} e^{-\Delta\tau \mathcal{H}_0} | S_l^z \rangle = \Lambda^N e^{-\Delta\tau J_1 \sum_{\langle i,j \rangle} S_{i,l}^z S_{j,l}^z - \Delta\tau J_2 \sum_{\langle\langle i,j \rangle\rangle} S_{i,l}^z S_{j,l}^z + \gamma \sum_i S_{i,l}^z S_{i,l+1}^z} \quad (\text{S5})$$

with $\gamma = -\frac{1}{2} \ln \tanh(\Delta\tau h)$, $\Lambda^2 = \sinh(\Delta\tau h) \cosh(\Delta\tau h)$. For a certain configuration $\{S_{i,l}^z\}$, the configurational weight is,

$$\omega\{S_{i,l}^z\} = \left(\prod_l \prod_{\langle i,j \rangle} e^{-\Delta\tau J_1 S_{i,l}^z S_{j,l}^z} \right) \left(\prod_l \prod_{\langle\langle i,j \rangle\rangle} e^{-\Delta\tau J_2 S_{i,l}^z S_{j,l}^z} \right) \left(\prod_\tau \prod_{\langle l,l' \rangle} \Lambda e^{\gamma S_{i,l}^z S_{i,l'}^z} \right). \quad (\text{S6})$$

Now, the 2D quantum problem becomes a (2+1)D classical Ising model, which can be solved by local or global update schemes, both adopted in our practical Monte Carlo samplings.

Within this framework, the physical observables can be evaluated as

$$\langle \hat{O} \rangle \approx \frac{1}{N} \sum_p^N \hat{O}(\{S_i\}_p) \quad (\text{S7})$$

where $\{S_i\}_p$ denotes the spin configurations in which the measurement is performed at the time p of Markov chain. Besides, we are also interested in the imaginary time spin-spin correlation function,

$$S(\mathbf{q}, \tau) = \frac{1}{N} \sum_{i,j} e^{i\mathbf{q} \cdot \mathbf{r}_{ij}} \langle S_i^z(\tau) S_j^z(0) \rangle, \quad (\text{S8})$$

which should be calculated in prior to the spin spectrum $S(\mathbf{q}, \omega)$. The latter can be obtained after a stochastic analytical continuation, as detailed in the Methods part.